# Observationally derived and general circulation model simulated tropical stratospheric upward mass fluxes

Qiong Yang,[1] Qiang Fu,[1] John Austin,[2] Andrew Gettelman,[3] Feng Li,[4] and Holger Vömel[5]

Received 8 February 2008; revised 8 July 2008; accepted 4 August 2008; published 30 October 2008.

[1] We quantify the vertical velocity and upward mass flux in the tropical lower stratosphere on the basis of accurate radiative heating rate calculations using 8-year Southern Hemisphere Additional Ozonesondes balloon-borne measurements of temperature and ozone and cryogenic frost-point hygrometer measured water vapor in the tropics (15°S—10°N). The impact of tropospheric clouds on the stratospheric heating rates is considered using cloud distributions from the International Satellite Cloud Climatology Project. We find a nearly constant annual mean upward mass flux in the tropical lower stratosphere above the top of the tropical tropopause layer (i.e., ~70 hPa), which is $1.13 \pm 0.40$ kgm$^{-2}$d$^{-1}$ for the 40- to 30-hPa layer, and $0.89 \pm 0.48$ kgm$^{-2}$d$^{-1}$ for the 70- to 50-hPa layer. A strong seasonal cycle exists in the upward mass flux and it is found that the mass flux below ~70 hPa is decoupled from that above in the Northern Hemisphere summer. Simulations of the tropical lower stratosphere from two stratospheric General Circulation Models (GCMs) are compared with observations. The annual mean upward mass fluxes from both GCMs for the 40- to 30-hPa layer agree well with observations, while the simulated mass fluxes for the 70- to 50-hPa layer are twice as large. Both GCMs also simulate seasonal variation of the mass flux reasonably well but are incapable of simulating the observed interannual variability of the upward mass flux, which is closely correlated with the quasi-biennial oscillations.

**Citation:** Yang, Q., Q. Fu, J. Austin, A. Gettelman, F. Li, and H. Vömel (2008), Observationally derived and general circulation model simulated tropical stratospheric upward mass fluxes, *J. Geophys. Res.*, *113*, D00B07, doi:10.1029/2008JD009945.

## 1. Introduction

[2] The Brewer-Dobson circulation (BDC) is the Lagrangian-mean mass circulation in the stratosphere, first described by *Brewer* [1949] and *Dobson* [1956] to explain stratospheric distributions of water vapor and ozone. This large-scale circulation consists of a meridional cell in each hemisphere with air rising across the tropical tropopause, moving poleward, and sinking toward the extratropical troposphere. The BDC is driven remotely by planetary and gravity wave breaking in the extratropical stratosphere, which acts like a ''suction pump'' drawing air upward from the tropics [*Haynes et al.*, 1991; *Holton et al.*, 1995]. The synoptic-scale wave breaking may also play a role in driving the BDC [*Plumb*, 2002; *Randel et al.*, 2002]. Since wave activity is stronger in the winter hemisphere than in the summer hemisphere and is stronger in the northern hemisphere (NH) than in the southern hemisphere (SH), the BDC is strongest in the NH winter [*Rosenlof and Holton*, 1993; *Holton et al.*, 1995]. GCMs predict an increase in the strength of the BDC, in response to an increase in wave activity associated with an increase of greenhouse gas concentrations as well as ozone depletion [e.g., *Rind et al.*, 1998; *Butchart and Scaife*, 2001; *Butchart et al.*, 2006; *Eichelberger and Hartmann*, 2005; *Li et al.*, 2008].

[3] The slow but continuous BDC plays a significant role in the stratosphere-troposphere-exchange of different chemical species, in the radiative energy balance, and consequently global climate change [e.g., *Holton et al.*, 1995; *Kley et al.*, 2000]. It is therefore critically important to have a quantitative estimate of the strength of the BDC based on observations, and to test and validate GCM simulations of the BDC. However, the BDC cannot be directly observed, since it describes the Lagrangian motion [e.g., *Rosenlof*, 1995]. In past studies, a variety of methods and calculations based on indirect measurements have been employed to evaluate the vertical velocities and mass fluxes associated with the BDC. One approach is based on the Transformed Eulerian-mean (TEM) zonal momentum and continuity equations which, under suitable conditions, can be used to derive the mean vertical velocity integrated cross the tropics. The TEM calculations can be based on meteorological analyses [e.g., *Rosenlof and Holton*, 1993; *Randel et al.*, 2002]. The largest restriction of this method is that it requires knowledge of all wave forcings, including subgrid-

[1]Department of Atmospheric Sciences, University of Washington, Seattle, Washington, USA.
[2]Geophysical Fluid Dynamics Laboratory, Princeton, New Jersey, USA.
[3]National Center for Atmospheric Research, Boulder, Colorado, USA.
[4]Goddard Earth Sciences and Technology Center, University of Maryland, Baltimore County, Baltimore, Maryland, USA.
[5]Cooperative Institute for Research in Environmental Sciences, University of Colorado, Boulder, Colorado, USA.


0148-0227/08/2008JD009945

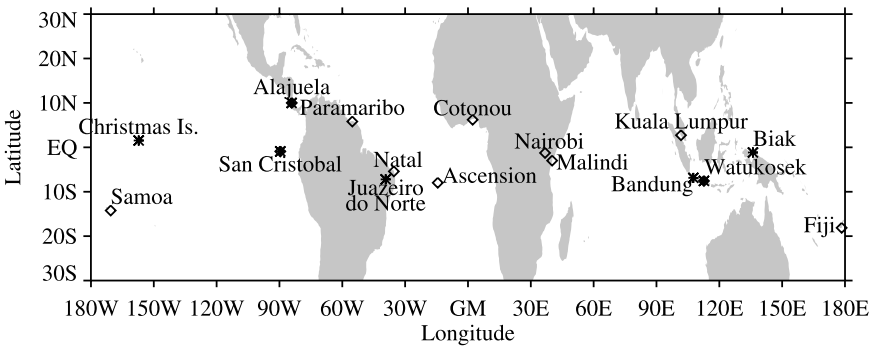


**Figure 1.** Locations of twelve SHADOZ sites (diamonds) and seven stations (asterisks) where water vapor profiles were obtained.

scale forcings (e.g., gravity wave drag) which are difficult to estimate accurately. Another method using the TEM framework estimates the residual vertical velocity and tropical upward mass flux by solving the TEM thermodynamic and continuity equations where the radiative heating rates are derived from a radiative transfer model using satellite and assimilated data [e.g., *Rosenlof*, 1995; *Eluszkiewicz et al.*, 1996; *Randel et al.*, 2002]. The vertical velocity of the BDC can also be inferred from the ascent rate of trace gases on the basis of satellite observations [e.g., *Mote et al.*, 1998; *Niwano et al.*, 2003].

[4] In this study we will use the TEM thermodynamic equation to provide an accurate estimate of the upward mass flux of the BDC in the tropical lower stratosphere based on observations [*Folkins et al.*, 2006; *Randel et al.*, 2007]. As opposed to previous studies, we use 8-year balloon-borne observations of atmospheric profiles from the Southern Hemisphere Additional Ozonesondes (SHADOZ) network (Figure 1) along with cloud distributions from the International Satellite Cloud Climatology Project (ISCCP) in the radiative transfer calculations with a validated radiative transfer model. Profiles of the vertical velocity and upward mass flux are derived from radiative heating rates. The annual, seasonal and interannual variations of the upward mass flux of the BDC are investigated and are compared with simulations from two GCMs with a well-resolved stratosphere.

## 2. Method of Observational Analysis

### 2.1. Vertical Velocity and Mass Flux

[5] The TEM residual circulation [e.g., *Andrews et al.*, 1987] is often used to estimate the zonally averaged transport of mass in the lower stratosphere. The mean meridional circulation ($\bar{v}^*$, $\bar{w}^*$) can be derived by solving the thermodynamic and continuity equations [e.g., *Solomon et al.*, 1986; *Rosenlof*, 1995; *Eluszkiewicz et al.*, 1996; *Randel et al.*, 2002]. The TEM thermodynamic equation [e.g., *Rosenlof*, 1995] is given by

$$\frac{\partial\overline{\theta}}{\partial t}+\overline{v}^*\frac{\partial\overline{\theta}}{\partial y}+\overline{w}^*\frac{\partial\overline{\theta}}{\partial z}=\frac{\overline{\theta}}{\overline{T}}\overline{Q}-\frac{1}{\rho_0}\frac{\partial}{\partial z}\left[\rho_0\left(\overline{v'\theta'}\frac{\overline{\theta}_y}{\overline{\theta}_z}+\overline{w'\theta'}\right)\right], \quad (1)$$

where $\theta$ is the potential temperature, $T$ the temperature, $Q$ the diabatic heating in terms of rate of change of temperature, and the overbar represents a zonal mean. The three terms on the left side of equation (1) are the potential temperature time tendency and meridional and vertical advections, respectively. The second term on the right side is the eddy flux divergence term.

[6] *Rosenlof* [1995] showed that the time tendency, meridional advection and eddy flux divergence terms in equation (1) are negligible in the tropical stratosphere. Therefore equation (1) can be simplified as

$$\overline{w}^*\frac{\partial\overline{\theta}}{\partial z}\frac{\overline{T}}{\overline{\theta}}=\overline{Q}. \quad (2)$$

Above the tropical tropopause, latent heat release is negligible, and thus radiative heating becomes dominant. By replacing $Q$ with radiative heating rate $Q_R$, equation (2) can be rewritten as

$$\overline{w}^*\frac{\partial\overline{\theta}}{\partial z}\frac{\overline{T}}{\overline{\theta}}=\overline{Q_R}. \quad (3)$$

The vertical velocity ($\bar{w}^*$) can then be derived from equation (3) by calculating $Q_R$ from a radiative transfer model with observed atmospheric profiles and cloud fields as inputs. For a given level, the vertical mass flux ($\overline{F}_{mass}$) is derived from

$$\overline{F}_{mass}=\rho\overline{w}^*, \quad (4)$$

where $\rho$ is the zonal mean air density.

### 2.2. Radiative Transfer Model

[7] In this study, the radiative heating rate, $Q_R$, is calculated using the NASA Langley Fu-Liou radiative transfer model [*Fu and Liou*, 1992, 1993; *Fu*, 1996; *Fu et al.*, 1998; *Rose and Charlock*, 2002]. The radiative transfer scheme is based on the delta-four-stream method for both solar and infrared spectra [*Liou et al.*, 1988; *Fu and Liou*, 1993] divided into six and twelve bands, respectively. The correlated k-distribution method is used to parameterize the nongray gaseous absorption by $H_2O$, $CO_2$, $O_3$, $N_2O$ and $CH_4$ [*Fu and Liou*, 1992] with the addition of CFCs and $CO_2$ in the window region [*Kratz and Rose*, 1999]. The $H_2O$ continuum absorption, CKD2.4 [*Tobin et al.*, 1999], is included in the whole thermal infrared spectra (0–

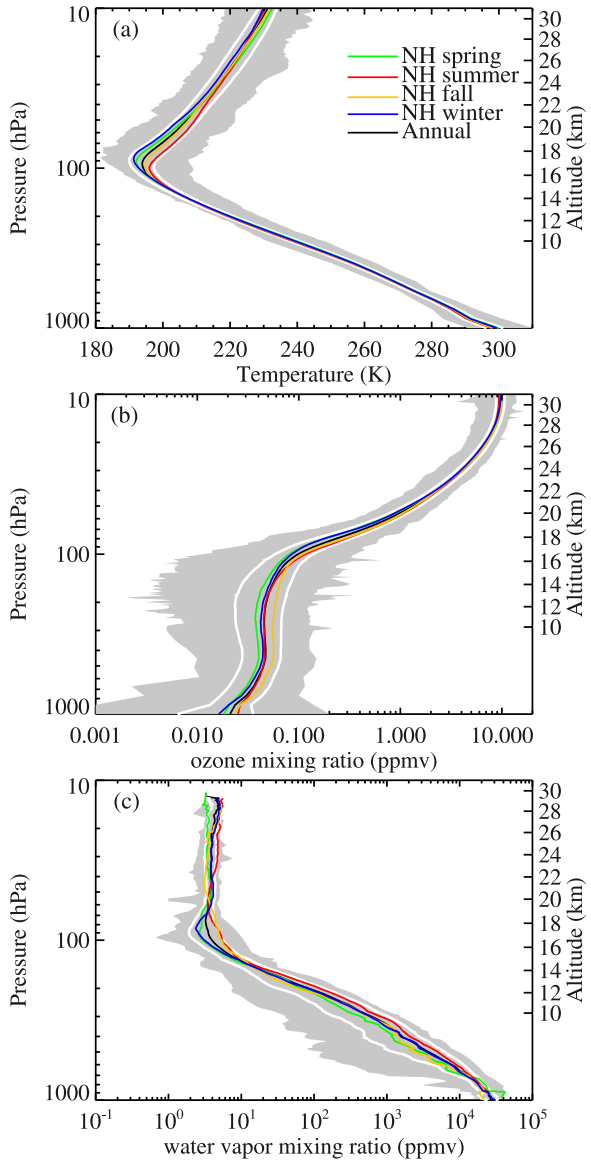


**Figure 2.** Balloon-borne observations of 2198 profiles of (a) temperature and (b) ozone from twelve SHADOZ sites (Figure 1) and (c) 137 profiles of water vapor from seven tropical stations (Figure 1). Gray shaded regions are the region of the observed temperature, ozone and water vapor; white lines are ±1 standard deviation; black lines are the annual mean; and green, red, gold, and blue lines are the seasonal mean for the NH spring (March–May), NH summer (June–August), NH fall (September–November) and NH winter (December–February), respectively.

2850 $cm^{-1}$). The modifications affecting the solar radiation include an inclusion of $O_2$ and $CO_2$ absorption [*Chou and Suarez*, 1999] and the minor absorption by $NO_2$, CO, NO, $SO_2$, $NH_3$, and $HNO_3$ etc, based on MODTRAN4. For water clouds, the single-scattering properties are parameterized on the basis of Mie calculations using liquid water content and mean effective radius [*Slingo*, 1989]. For ice clouds, the single-scattering properties are parameterized using ice water content and a generalized effective particle size [*Fu*, 1996; *Fu et al.*, 1998]. The difference of heating rates between the Fu-Liou model and line-by-line calculations is less than about 0.04 K/d in the upper troposphere and lower stratosphere [*Fu and Liou*, 1992; *Gettelman et al.*, 2004].

## 3. Observations of Temperature, Ozone, and Water Vapor

### 3.1. Temperature and Ozone Profiles

[8] A total of 2198 simultaneously measured temperature (Figure 2a) and ozone (Figure 2b) profiles of at least up to 28 km (~16 hPa) are obtained from twelve SHADOZ stations (Figure 1) located within about 15°S–10°N during the period 1998–2005 [*Thompson et al.*, 2003]. The results shown in this paper will be the zonal and latitudinal average in the tropics over the region of 15°S–10°N. The mean cold point tropopause height is about 16.9 km (Figure 2a). The cold point tropopause varies seasonally, and is highest in the NH winter (~17.3 km) and lowest in the NH summer (~16.6 km).

[9] In order to obtain accurate radiative heating rate calculations below 30 km, the profiles are extended up to 0.2 hPa. Above the sounding level, the United Kingdom Meteorological Office (UKMO) monthly stratospheric analysis temperature data and HALogen Occultation Experiment (HALOE) monthly ozone data are used [*Swinbank and O'Neill*, 1994; *Russell et al.*, 1993; *Gettelman et al.*, 2004]. Blending of the temperature and ozone profiles occurs over the uppermost ~3 km of each sounding. Within this range, the temperature and ozone mixing ratio are constructed following *Hollars* [2004],

$$VAR(\ln p) = W \cdot VAR_{UKMO/HALOE}(\ln p) + (1 - W) \cdot VAR_{balloon-borne}(\ln p), \quad (5)$$

where VAR is either the temperature or the ozone mixing ratio, and the subscripts indicate the values from the SHADOZ balloon-borne observations, or from the climatological UKMO/HALOE data. $W$ is a weighting function defined as

$$W(\ln p) = \frac{\ln p - \ln p_{bottom}}{\ln p_{top} - \ln p_{bottom}}, \quad (6)$$

where $p_{top}$ and $p_{bottom}$ are the pressures at the top and bottom of the upper 3 km range of each sounding. In the radiative transfer calculations, a vertical resolution of 100 m is used between 10 km and 30 km. Below 10 km and above 30 km, a resolution of 1 km is used. Figure 3 depicts an example of the blending of individual temperature and ozone sounding profiles with UKMO/HALOE climatological data.

### 3.2. Water Vapor Profiles

[10] A total of 137 water vapor profiles (Figure 2c) measured by the cryogenic frost-point hygrometer (CFH) as well as the NOAA/CMDL (now NOAA/ESRL) frost-point hygrometer balloon soundings from seven tropical stations (Figure 1) are used. The available number of water vapor profiles from individual station is listed in Table 1. These observations were obtained by the Soundings of Ozone and Water in Equatorial Regions (SOWER) project

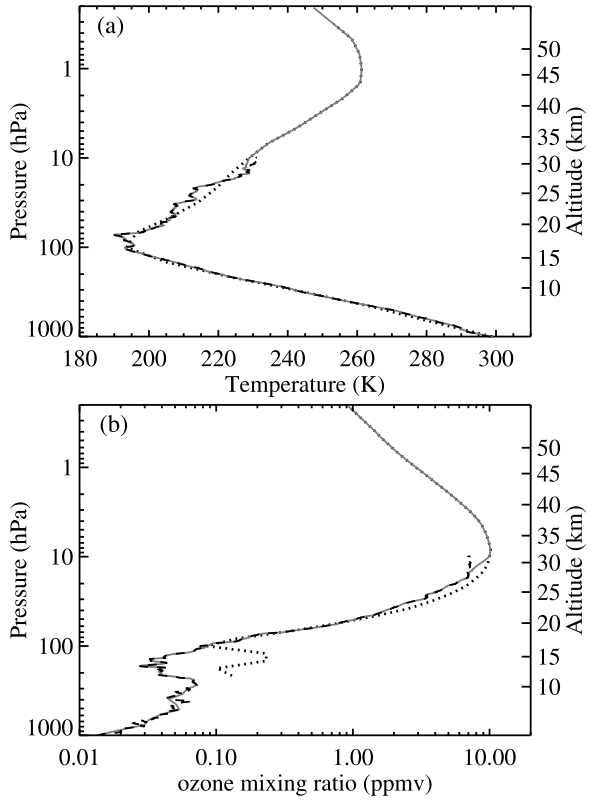


**Figure 3.** A demonstration of construction of profiles of temperature and ozone mixing ratio input to the Fu-Liou model. (a) Temperature. Sounding profile is black dashed line; UKMO monthly mean temperature is black dotted line. (b) Ozone mixing ratio. Sounding profile is black dashed line; HALOE monthly data are black dotted line. The merged profiles are shown in gray solid lines.

[*Hasebe et al.*, 1999], the Atmospheric InfraRed Sounder (AIRS) and AURA satellite validation measurements, as well as the Observations of the Middle Stratosphere (OMS) experiment. Among those profiles, there are 25 profiles from the NH spring, 37 profiles from the NH summer, 20 profiles from the NH fall and 55 profiles from the NH winter. Because not all of these 137 profiles go up to the lower stratosphere, a different blending method is applied to make full use of these high-quality water vapor soundings.

[11] To account for the seasonal variation of water vapor, four seasonal mean water vapor profiles (up to 14 hPa) from the balloon-borne measurements are constructed (Figure 4 below point B). These profiles are obtained by averaging all available water vapor soundings at each level for a given season. The four profiles are then merged with the HALOE seasonal mean water vapor profiles (Figure 4 above point A): The water vapor mixing ratios between A and B which are 3 km apart are obtained through linear interpolation in log-pressure coordinate. As the temperature and ozone profiles, these four merged seasonal water vapor profiles have a vertical resolution of 100 m between 10 km and 30 km and 1 km elsewhere. Figure 4 shows that at the cold point tropopause, water vapor exhibits minima in the NH winter and spring in response to the lower cold point temperatures in these two seasons.

**Table 1.** Number of Water Vapor Profiles Available From Seven Stations

| Station | Number of Water Vapor Profiles |
|---|---|
| Alajuela | 67 |
| Bandung | 12 |
| Biak | 8 |
| Christmas Is. | 13 |
| Juazeiro do Norte | 2 |
| San Cristobal | 28 |
| Watukosek | 7 |

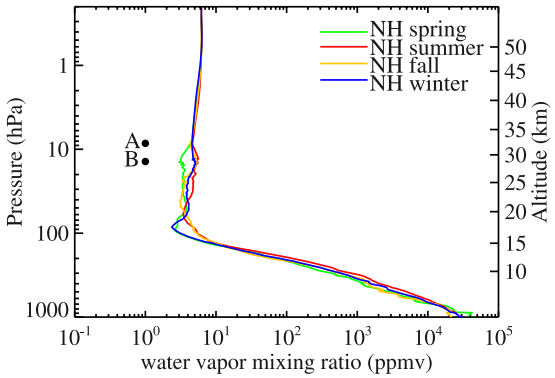


**Figure 4.** Merged seasonal mean water vapor profiles. Below point B: the seasonal mean profiles from soundings. Above point A: the seasonal mean profiles from HALOE. Four straight lines between point A and point B are used to connect sounding data and HALOE data.

[12] Owing to the limited availability of high-quality frost-point hygrometer water vapor measurements, we only use the seasonal mean water vapor profiles in the radiative transfer calculations. *Corti et al.* [2005] found that the radiative heating rate in the tropical upper troposphere and lower stratosphere using the mean water vapor profiles differs from that based on individual water vapor profiles by less than 0.01 K/d. More high-quality water vapor soundings are needed in the future to derive reliable monthly mean water vapor profiles.

### 3.3. Cloud Fields

[13] The impact of tropospheric clouds on the stratospheric radiative heating rates is significant [*Fueglistaler and Fu*, 2006]. Considering the temporal and spatial variations of clouds, we use annually varying monthly mean cloud fields constructed from the ISCCP D1 data set [*Rossow and Schiffer*, 1999], which contains cloud fractions for 42 cloud types categorized according to seven cloud top pressure bins (10–180–310–440–560–680–800–1000 hPa) and six cloud optical depth bins (0.02–1.27–3.55–9.38–22.63–60.36–378.65) with a spatial resolution of 2.5° × 2.5°.

[14] We use the ISCCP cloud fields in the radiative transfer calculation following *Hartmann et al.* [2001]. Since ISCCP couldn't distinguish multiple layers of clouds, all 42 cloud types are assumed to be single cloud layers with vertical cloud extent following climatological values [*Liou*, 1993]. Seven bin midpoint cloud top pressures (130, 245, 375, 500, 620, 740 and 900 hPa) and six bin midpoint cloud

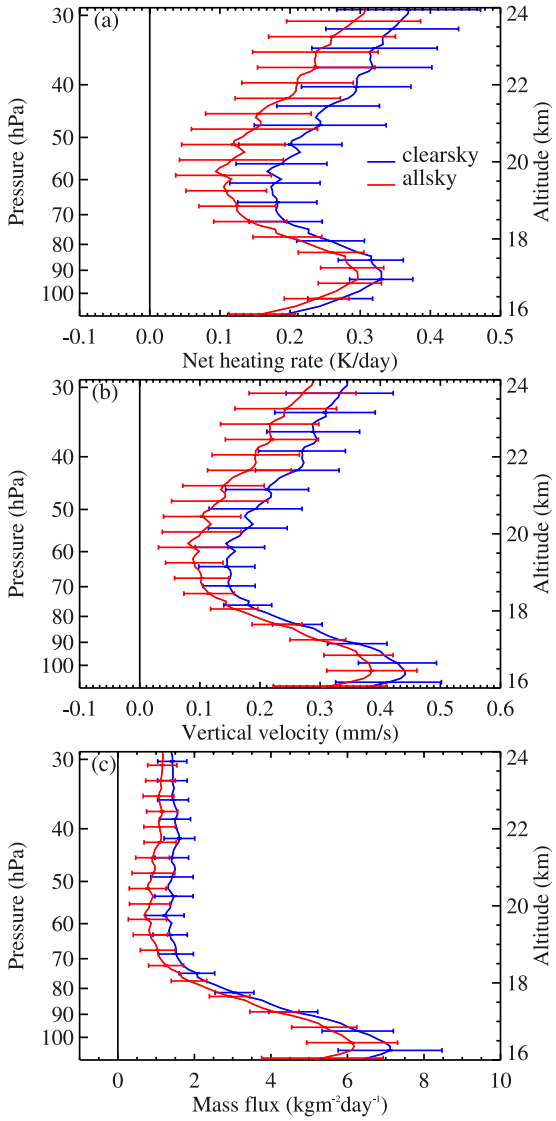


**Figure 5.** (a) The annual mean radiative heating rates for 1998–2005, (b) the mean vertical velocity, and (c) the mean upward mass flux. Blue lines are results for clear-sky and red lines are results for all-sky conditions.

optical depths (0.65, 2.41, 6.46, 16.0, 41.5 and 219.5) are used for the calculation. Clouds above 560 hPa are assumed to be ice clouds with a mean effective ice particle size of 30 $\mu$m. Clouds below 560 hPa are assumed to be liquid with a mean effective water droplet radius of 10 $\mu$m. *Hartmann et al.* [2001] showed that the simulated reflected solar radiation and outgoing longwave radiation using the Fu-Liou radiation model along with ISCCP data agree well with the observations from the Earth Radiation Budget Experiment (ERBE). Thus the impact of tropospheric clouds on the stratospheric radiative heating rates should be appropriately considered by using the ISCCP data.

[15] In this study, we did not consider clouds above 16 km. *Fu et al.* [2007] showed that total cloud fractions in the tropical region are about 15% at 16 km, 5% at 17 km, and 0.5% at 18 km, which are dominated by thin and subvisible cirrus clouds. These clouds would lead to substantial heating at the levels where the clouds occur but have little impact on the radiative heating rates above them [*Fueglistaler and Fu*, 2006]. The impact of thin and subvisible cirrus on the radiative heating rates between 16 and 18 km will be quantified in a future study using the cloud information from Cloud-Aerosol Lidar and Infrared Pathfinder Satellite Observation (CALIPSO).

[16] In the radiative transfer calculations, the solar surface albedo and thermal surface emissivity are set to be 0.07 and 0.99, respectively. The monthly and latitudinal dependences of insolation are considered for twelve SHADOZ sites and the diurnal variation of solar radiation is taken into account explicitly. In the radiative transfer calculations we use the average values between 1998 and 2005 for the concentrations of chemical species including $CO_2$ (372 ppmv), $CH_4$ (1.775 ppmv), $N_2O$ (0.316 ppmv), CFC-11 (0.26 ppbv), CFC-12 (0.535 ppbv) and CFC-22 (0.15 ppbv).

## 4. Radiative Heating Rate, Vertical Velocity, and Mass Flux Derived From Observations

[17] By inputting 2198 temperature and ozone profiles along with four seasonal mean water vapor profiles to the radiative transfer model, we obtain 2198 clear-sky radiative heating rate profiles. For a given pair of atmospheric temperature and ozone profiles, we derive the radiative heating rate in all-sky conditions from

$$Q_R = \sum_{i=1}^{42} C_i Q_{R,i} + (1 - C) Q_{R,clear}, \tag{7}$$

where $C_i$ is the cloud fraction for each cloud type, $C = \sum_{i=1}^{42} C_i$ is the total cloud fraction and $Q_{R,clear}$ and $Q_{R,i}$ are the radiative heating rates for the clear sky and cloudy sky (with the cloud type $i$), respectively. Thus we also obtain 2198 all-sky radiative heating rate profiles. Figure 5 shows the annual mean profiles of the zonally and latitudinally averaged heating rate (Figure 5a) and the derived vertical velocity (from equation (3)) (Figure 5b) and upward mass flux (from equation (4)) (Figure 5c) for clear-sky (blue lines) and all-sky (red lines) conditions for 1998–2005. Figure 6 is the same as Figure 5 except that seasonal mean profiles are displayed. Since the spatial distribution of 12 SHADOZ stations over the tropics is nearly zonally uniform (Figure 1), the profiles in Figures 5 and 6 can be considered as the zonally averaged values between 15°S and 10°N. The error bars in Figures 5 and 6 represent the 2-standard deviation ($2\acute{o}$) uncertainties in the derived quantities. In the following, we first discuss the estimate of uncertainties in the radiative heating rates (section 4.1), which are translated to the uncertainties in the derived vertical velocity and mass flux through equation (3) and (4). We then discuss the annual mean and seasonal mean profiles in Figures 5 and 6, respectively, in sections 4.2 and 4.3.

### 4.1. Uncertainties in Estimated Radiative Heating Rates

[18] The uncertainties in the calculated mean radiative heating rates are caused by measurement errors of input temperature, ozone and water vapor, errors associated with the radiative transfer model, and the standard error of the

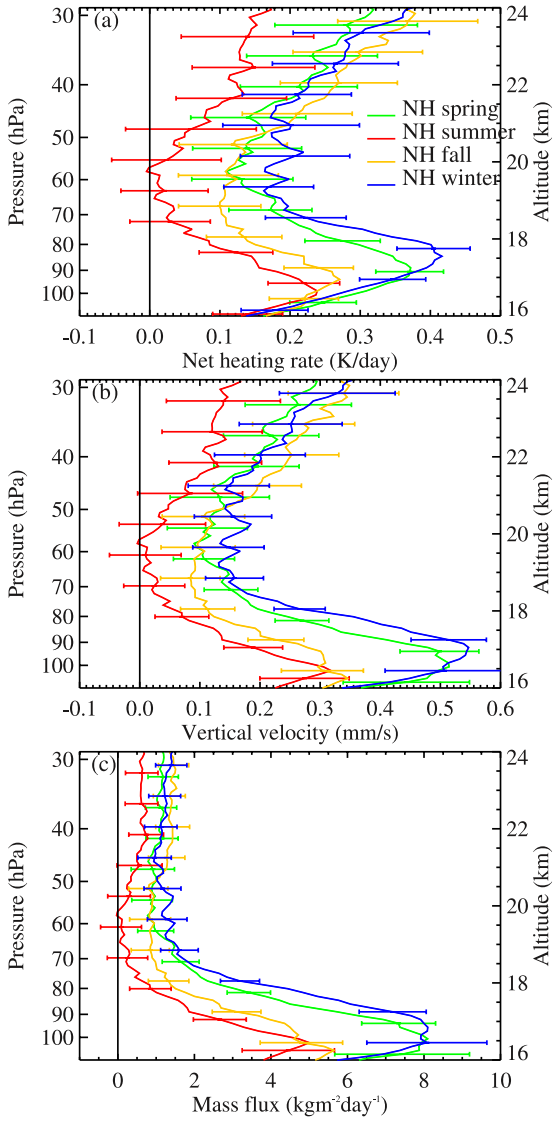


**Figure 6.** Same as Figure 5 but for seasonal mean profiles. Green: the NH spring (March–May); red: the NH summer (June–August); gold: the NH fall (September–November); blue: the NH winter (December–February).

heating rate profiles related to natural variations. The errors in measured temperature, ozone, and water vapor are appropriately ±0.3 K, ±5%, and ±10%, respectively, at the 1ó uncertainty level [*Thompson et al.*, 2003; *Vömel et al.*, 2002]. (Note that the SHADOZ ozone measurement has its greatest uncertainty in the lower stratosphere because of relatively high signal-to-noise ratio and the uncertainty may vary from one station to another [*Smit et al.*, 2007; *Thompson et al.*, 2007].) The corresponding error in radiative heating rate ($\sigma_T, \sigma_{O3}, \sigma_{H2O}$) due to the 1ó uncertainty ($\Delta x$) in $T$, $O_3$, or $H_2O$ measurement is estimated according to the Upper-Lower Bounds method,

$$\sigma_x(z) = \max\{|Q_R[\bar{x}(z) + \Delta x] - Q_R[\bar{x}(z)]|, |Q_R[\bar{x}(z) - \Delta x] - Q_R[\bar{x}(z)]|\}, \quad (8)$$

where $\bar{x}(z)$ is the mean vertical profile of temperature, ozone, or water vapor. The error associated with radiative transfer model, ó$_R$, is about 0.02 K/d (68% or 1ó confidence level). The standard error of the radiative heating rates is $\sigma_{QR}/\sqrt{N-1}$ where $N$ is the number of heating rate profiles used to derive the mean and $\sigma_{QR}$ is the standard deviation of the $N$ radiative heating rate profiles. By assuming that these errors are independent, the total uncertainties in the derived mean radiative heating rate is

$$\sigma(z) = \sqrt{\sigma_T^2(z) + \sigma_{O_3}^2(z) + \sigma_{H_2O}^2(z) + \sigma_R^2(z) + \frac{\sigma_{Q_R}^2(z)}{N-1}}, \quad (9)$$

where N = 2198, 543, 533, 609, and 513 for annual mean, winter, spring, summer, and fall seasonal means, respectively. Figure 7 presents the *ó* profile along with its individual components, $\sigma_T$, $\sigma_{H2O}$,$\sigma_{O3}$, $\sigma_R$, and $\sigma_{QR}/\sqrt{N-1}$ (see equation (9)). The error related to temperature measurement is small (except for the region from 20 to 20.5 km), as well as the standard error. Below 70 hPa (∼18.5 km), the error associated with the radiative transfer model dominates, while above 45 hPa (∼21 km), the error due to $O_3$ is largest. In between, the errors due to $H_2O$, $O_3$, and radiative transfer modeling are comparable. The uncertainties in the derived vertical velocity and mass flux are derived from the uncertainty in the radiative heating rate through equations (3) and (4). The error bars shown in Figures 5 and 6 are ±2$\sigma$ (95% confidence level).

### 4.2. Annual Mean Profiles

[19] The annual mean radiative heating rate profiles are shown in Figure 5a, and exhibit an "S" like shape with a maximum around the cold point tropopause, and a minimum in the region between ∼18.5 and ∼19.5 km (70–60 hPa). The cloud top temperatures, especially those of high thick clouds are much lower than the surface temperatures, resulting in less infrared heating in the lower stratosphere. At the same time, clouds enhance the solar heating in the lower stratosphere by reflecting more solar radiation. Figure 5a shows that the net impact of clouds reduces the radiative heating rates by about 0.05 to 0.08 K/d between 18.5 and 24 km (70–30 hPa), the so-called

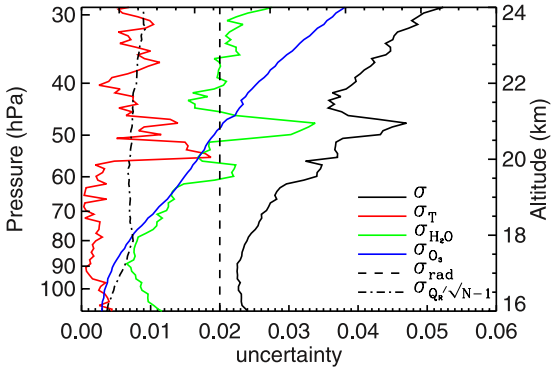


**Figure 7.** One-$\sigma$ uncertainties in estimated radiative heating rates for annual mean all-sky conditions, due to observational errors and error in radiative transfer calculations.

**Table 2.** Annual Mean Upward Mass Fluxes in the Lower Stratosphere From Observational Analysis and Two GCMs[a]

| | Observations: Clear-Sky | Observations: All-Sky | NCAR/WACCM3 | GFDL/AMTRAC |
|---|---|---|---|---|
| 30–40 hPa (22–24 km) | 1.46 ± 0.40 | 1.13 ± 0.40 | 1.37 | 1.18 |
| 50–70 hPa (18.5∼20.5 km) | 1.41 ± 0.48 | 0.89 ± 0.48 | 1.95 | 1.95 |

[a]Unit is kg $m^{-2}$ $d^{-1}$.

stratospheric "tropical pipe" region [*Plumb*, 1996]. This result agrees well with *Fueglistaler and Fu* [2006] who used cloud fields from ground-based millimeter cloud radars at tropical Manus and Nauru sites. Note that the radiative heating rates may be significantly underestimated between 16 and 17 km without considering thin and subvisible cirrus clouds. (Such underestimation decreases rapidly with height and becomes negligible above 18 km.)

[20] Figure 5b shows the vertical velocity profiles (from equation (3) using $Q_R$ from equation (7)). At 100 hPa (∼16.5 km), the all-sky vertical velocity is 0.38 ± 0.07 mm/s, in reasonable agreement with the results of *Randel et al.* [2002], *Eluszkiewicz et al.* [1996] and *Rosenlof* [1995]. Since all these studies (including the present one) do not consider the impact of thin cirrus clouds, the vertical velocity at 100 hPa may be underestimated. Above 100 hPa, the all-sky vertical velocity decreases with height to a minimum of 0.1 ± 0.05 mm/s at ∼70 hPa and then increases with height above ∼60 hPa. At 30 hPa, the all-sky vertical velocity is 0.29 ± 0.09 mm/s. The shape of vertical velocity profiles shown in Figure 5b is similar to that from *Rosenlof* [1995] [see *Mote et al.*, 1998, Figure 1].

[21] The all-sky upward mass flux, as shown in Figure 5c, decreases above the cold point tropopause (∼100 hPa) to about 70 hPa, indicating a divergence of air masses. From 70 hPa to 30 hPa, the all-sky mass flux is nearly constant (nondivergent) which is the upwelling branch of the BDC in the tropical pipe region. The slight minimum between 19 and 21 km is largely caused by the decoupling of the BDC upward mass flux, driven by the planetary and gravity wave breaking, from the mass flux below in the summer season (see Figure 6).

[22] Within the tropical tropopause layer (TTL), the upward mass flux is not only driven by the planetary and gravity wave breaking, but also by the subtropical synoptic-scale wave breaking [*Plumb*, 2002], and by tropical tropospheric processes. The latter includes tropical convection and related wave activities [*Boehm and Lee*, 2003; *Kerr-Munslow and Norton*, 2006] as well as active large-scale diabatic heating associated with thin cirrus clouds [*Corti et al.*, 2005]. These influences could be as high as the top of the TTL which was identified by *Fu et al.* [2007] as at about 18.5 km (70 hPa). Therefore investigations of the stratospheric BDC need to consider values above 70 hPa, as indeed were done by *Butchart and Scaife* [2001] and *Butchart et al.* [2006].

[23] For the test of the GCM simulations of BDC, we will therefore focus on the region between 18.5 and 24 km (i.e., 70–30 hPa) in section 5. It should be also noted that our estimated upward mass flux near the cold point tropopause may be underestimated owing to the neglect of thin cirrus clouds in radiative transfer calculations. Table 2 shows that the annual mean upward fluxes are 1.13 ± 0.4 kg $m^{-2}$ $d^{-1}$ between 22 and 24 km (40–30 hPa), and 0.89 ± 0.48 kg $m^{-2}$ $d^{-1}$ between 18.5 and 20.5 km (70–50 hPa). The annual mean upward mass fluxes without considering the cloud radiative effect is about 1.43 kg $m^{-2}$ $d^{-1}$ (Table 2). The consideration of the ISCCP cloud fields results in a reduction of ∼30% in the upward mass flux between 22 and 24 km and ∼ 58% between 18.5 and 20.5 km, respectively.

### 4.3. Seasonal Mean Profiles

[24] Figure 6 illustrates the seasonal mean profiles of heating rate, vertical velocity and upward mass flux in all-sky conditions. These profiles all exhibit pronounced seasonal dependences, because of the dominant role played by temperature in determining the radiative heating rates and atmospheric vertical stability (see Figure 2a and equation (3)).

[25] The upward mass flux below 20.5 km (50 hPa) shows a maximum in the NH winter but a minimum in the NH summer. This indicates that the BDC is strongest in the NH winter and weakest in the NH summer, which is consistent with previous findings [e.g., *Rosenlof*, 1995]. Above 20.5 km, the BDC is still weakest in the NH summer, but the heating rate, vertical velocity, and especially mass flux from the other three seasons are more comparable, with larger values in the NH fall season.

[26] It is notable that the upward mass flux in the NH summer has a near-zero minimum around 19–20 km and then increases from 20 km to 22 km, implying a convergence for the mass flux. The near-zero vertical mass flux suggests a decoupling of the BDC, driven by the planetary and gravity wave breaking, from the vertical mass flux below in the NH summer. We have examined the vertical mass fluxes within different latitudinal bands including 5°N–10°N, 5°S–5°N, and 15°S–5°S in the NH summer. The decoupling of the vertical mass flux is clearly seen around 60–70 hPa within all these latitudinal bands (not shown), which suggests that the mass flux decoupling in the NH summer is real. The reason for this behavior remains unknown and should be the subject of future research, along with its implication to the troposphere-to-stratosphere transport. It seems to be clear that in the NH summer the physical processes that drive the tropical upward mass flux below 19 km are very different from those above.

## 5. Comparisons Between Observations and Models

[27] In this section, we compare the BDC derived from observations with the results from two GCM simulations.

### 5.1. Model Descriptions

[28] The two GCMs used are the Geophysical Fluid Dynamics Laboratory (GFDL) Atmospheric Model with Transport and Chemistry (AMTRAC) and the National Center for Atmospheric Research (NCAR) Whole Atmosphere Community Climate Model Version 3(WACCM3).

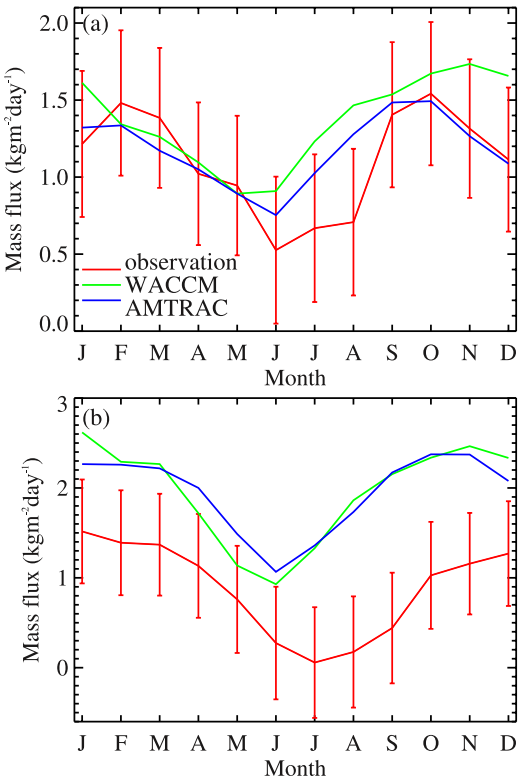


**Figure 8.** Monthly variations of upward mass fluxes (a) between 22 and 24 km (40 and 30 hPa) and (b) between 18.5 and 21.5 km (70 and 50 hPa) from the observation (red), WACCM3 (green), and AMTRAC (blue).

[29] AMTRAC is described by *Austin and Wilson* [2006] and is an extension of the GFDL Atmospheric Model (AM2) [*Anderson et al.*, 2004] with a coupled troposphere-stratosphere photochemistry scheme [*Austin and Butchart*, 2003]. It has 48 layers with the top pressure of 0.002 hPa and a horizontal grid spacing of 2° × 2.5°. The vertical resolution in the upper stratosphere is about 4 km, decreasing steadily to 1.5 km in the lower stratosphere. The parameterizations of the physical and radiative processes in AMTRAC are analogous to those of GFDL AM2 except that the dynamical core and tracer transport are based on finite volume numerical scheme [*Lin*, 2004]. The *Alexander and Dunkerton* [1999] scheme is implemented to parameterize nonorographic gravity wave forcing in the middle atmosphere. For the past runs (1960–2004) [*Eyring et al.*, 2006], observed time-dependent sea surface temperature, sea ice amounts, and concentrations of long-lived greenhouse gases are prescribed. Observed solar cycle variations are used to specify the radiative fluxes at the top of the atmosphere.

[30] WACCM3 is a coupled chemistry climate model that spans the atmosphere from the surface to the lower thermosphere (140 km). The model is described by *Garcia et al.* [2007]. The runs discussed in the present paper were made with horizontal resolution of 2° × 2.5° and a vertical resolution of about 1 km in the upper troposphere/lower stratosphere region. WACCM3 is based on the framework of the Community Atmosphere Model, version 3 (CAM3), described by *Collins et al.* [2006]. WACCM3 uses CAM3 as its base, and adds parameterizations for chemistry and upper atmospheric processes. The CAM model top is typically 2 hPa (45 km), while the WACCM model top is $5 \times 10^{-6}$ hPa (140 km). The chemistry module for WACCM3 is derived from the three-dimensional chemical transport Model for Ozone and Related chemical Tracers (MOZART) [*Brasseur et al.*, 1998; *Horowitz et al.*, 2003; *Kinnison et al.*, 2007]. The chemistry is coupled online to the model dynamics and radiation to have realistic model heating rates.

[31] We use vertically averaged mass fluxes between 22 and 24 km and between 18.5 and 20.5 km to evaluate the strength of BDC in the tropics. We compare the GCM simulations with observational analysis in terms of annual mean BDC and seasonal and interannual variations. Note that the GCM simulated vertical velocity is used to derive the GCM upward mass flux in the modeling analysis.

### 5.2. Annual Mean Upward Mass Flux

[32] Using equation (4), the simulated upward mass fluxes were determined from the zonal mean residual vertical velocity between 15°S and 10°N from the GCM past runs [*Eyring et al.*, 2006] for the period 1998—2004. Table 2 shows the annual mean upward mass fluxes from the two GCMs compared with observations. The GCM mass flux profiles exhibit the similar shape to that observed (not shown). The mass fluxes from both AMTRAC and WACCM3 agree well with observations for the 22- to 24-km layer. But for the layer between 18.5 and 20.5 km, the GCM results are twice as large as the values derived from observations.

### 5.3. Seasonal and Interannual Variations of the Mass Flux

[33] The monthly variations of upward mass fluxes are compared in Figure 8. The observations for the 22–24 km (40–30 hPa) layer (Figure 8a) have minima during June–August and December–January and maxima during September–October and February–March. For the layer between 18.5 and 20.5 (70–50 hPa), the mass flux has a minimum in the NH summer and a maximum from October to March (Figure 8b). *Randel et al.* [2002] showed that the extratropical wave forcing peaks during November–March in the NH and during September–November in the SH. Therefore the combined global wave forcing is relatively high from September to March. Figure 8 indicates that both AMTRAC and WACCM3 simulate the monthly variations of the BDC reasonably well and reproduce the observed transition from an annual variation at 70–50 hPa to a semiannual variation at 40–30 hPa.

[34] Figure 9 shows the interannual variations of the BDC from both models and observations for the 22- to 24-km layer for 1998–2005. Since these two GCMs do not simulate the quasi-biennial variation (QBO), the model results do not exhibit as much interannual variability as observed. The observed mass flux is highly correlated with the QBO, as illustrated in Figure 10, which shows a scatterplot between the yearly mean mass flux for 1998–2005 and the 12-month averaged zonal wind at 50 hPa based on ECMWF Re-Analysis (ERA-40) from October 1997 to September 2005. In Figure 10, the vertical mass

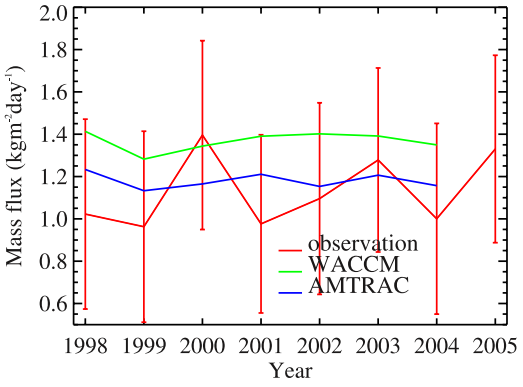


**Figure 9.** Interannual variation of upward mass fluxes between 22 and 24 km (40 and 30 hPa) from the observation (red), WACCM3 (green), and AMTRAC (blue).

fluxes were lagged by 3 months behind the zonal wind at 50 hPa. The correlated coefficient is high up to 0.94, which suggests that the interannual variation of the BDC is related to QBO [*Randel et al.*, 1999].

### 5.4. Temperature, Ozone, and Water Amounts

[35] As discussed in section 5.1, the mass fluxes from both GCMs agree well with observations for the 22- to 24-km layer. But for the layer between 18.5 and 20.5 km, the GCM results are twice as large as the values derived from observations. To gain further insight into GCM simulations of tropical lower stratosphere, we compare the simulated and observed temperatures and $H_2O$ and $O_3$ concentrations in Figure 11. One aspect of the results is that in the region (40–30 hPa) where the BDC is accurately simulated, the temperatures from both AMTRAC and WACCM3 are overpredicted by as much as 5 K (Figure 11a). This may be partly because the GCM radiation schemes overestimate the radiative heating rate there. *Gettelman et al.* [2004] showed that for given tropical atmospheric profiles, the heating rates near 23 km from the NCAR CAM radiation scheme are about 0.25 K/d larger

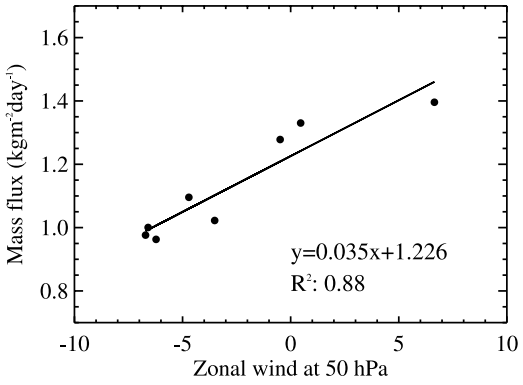


**Figure 10.** The scatterplot of the mass flux between 40 and 30 hPa versus zonal wind at 50 hPa. The *x* axis is 12-month averaged zonal wind at 50 hPa from the ECMWF starting from October 1997 to September 2005; and the *y* axis is 12-month averaged mass flux between 40 and 30 hPa, starting from January 1998 to December 2005.

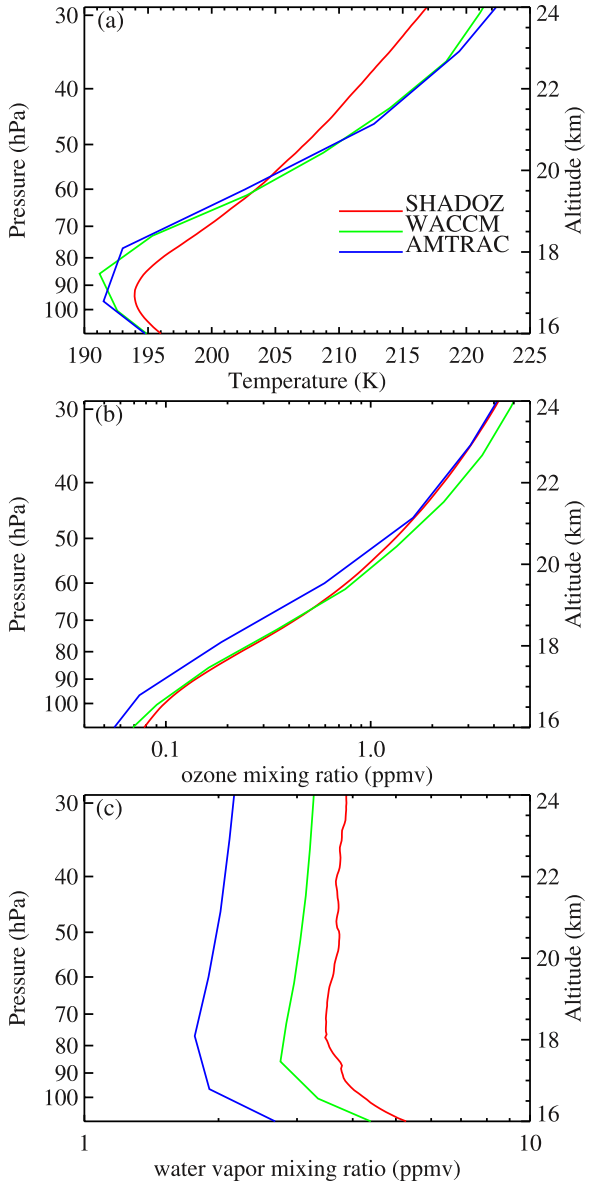


**Figure 11.** Annual mean (a) temperature, (b) ozone, and (c) water vapor, for 1998–2004, from the observation (red), WACCM3 (green), and AMTRAC (blue) in the tropical lower stratosphere.

than those from the Fu-Liou radiation model. The radiative heating rates, which are largely dominated by the temperature variation, passively respond to the dynamically driven BDC. Thus for the region with accurately simulated BDC, the biases in radiative heating rate calculations would directly lead to biases in temperature predictions.

[36] For the layer between 18.5 and 20.5 km where the simulated mass flux is significantly larger than the observed, the vertically averaged temperatures from AMTRAC and WACCM3 agree well with observations (Figure 11a). But both GCMs underestimate the $H_2O$ concentrations (Figure 11c), because the cold point tropopause temperatures are lower than observed (Figure 11a). Note that $H_2O$ and $O_3$ have radiative cooling and warming effects in the TTL, respectively [*Gettelman et al.*, 2004].

Thus the underestimation of $H_2O$ concentrations by the two GCMs causes a considerable radiative heating in the TTL. (AMTRAC also underestimates the $O_3$ concentration in the 18.5- to 20.5-km layer (Figure 11b). This would partly cancel the radiative warming owing to the underestimation of $H_2O$, resulting in a less radiative heating.) Therefore the larger radiative heating rates corresponding to larger simulated BDC (Table 2), are not only related to the biases in GCM radiation scheme (Gettelman et al. showed a difference of ~0.1 K/d at 19.5 km between CAM and Fu-Liou radiation models), but also related to the predicted biases in $H_2O$ and $O_3$ concentrations.

[37] We have examined the thermodynamic energy budget terms in equation (1) in the tropics (15°S–10°N) using the AMTRAC run for 1998–2004. For the 22- to 24-km layer, the temperature tendency, horizontal advection, and eddy mixing terms are negligible, and the radiative heating rates are exactly balanced by the dynamical cooling related to the vertical advection. At 18.5 km, however, although the temperature tendency term is still zero, the horizontal advection term provides a cooling of ~0.05 K/d, and the eddy mixing provides a cooling of about 0.15 K/d. If the large cooling (~0.2 K/d) associated with the eddy mixing and horizontal advection were real (we did not consider these terms in observational analysis), then the observed upward mass flux (see equation (1) and Figure 5a) at 18.5 km would become negative (~−0.08 mm/s), indicating an unphysical tropical "downwelling" of the BDC. Therefore we suggest that the significant cooling associated with eddy mixing and horizontal temperature advection may artificially be produced by numerical models. Further investigation on this subject is needed.

## 6. Summary and Conclusions

[38] Eight-year balloon-borne observations of temperature, ozone and water vapor in the tropics (15°S–10°N) complemented with ISCCP cloud information during the same period are used to quantify the vertical velocity and upward mass flux in the lower stratosphere. We find near-constant annual mean upward mass fluxes in the stratospheric pipe region between 70 and 30 hPa (i.e., 18.5–24 km). The annual mean mass flux is 1.13 ± 0.40 and 0.89 ± 0.48 kg/m$^2$/d, respectively, for the layers between 40 and 30 hPa (22–24 km) and between 70 and 50 hPa (18.5–20.5 km). By including the cloud fields in the radiative transfer calculations, the upward mass flux is reduced by ~30% between 40 and 30 hPa and ~ 58% between 70 and 50 hPa, respectively. Below the top of the tropical tropopause layer (i.e., ~70 hPa or 18.5 km), the upward mass flux, which is contributed by both Brewer-Dobson circulation (BDC) and those directly associated with tropical tropospheric processes, decreases with height. It is found that the uncertainties in the observational analyses of the upward mass fluxes are mainly caused by the measurement errors in $O_3$ and $H_2O$ and the errors in the radiative transfer model.

[39] As in previous studies [e.g., *Rosenlof and Holton*, 1993; *Eluszkiewicz et al.*, 1996; *Randel et al.*, 2002; *Butchart et al.*, 2006; *Li et al.*, 2008], a strong seasonal cycle exists in both vertical velocity and upward mass flux of the BDC with a minimum in the NH summer. It is found that the BDC mass flux in the NH summer is decoupled from the vertical mass flux below. The reason for this decoupling and its implication to the troposphere-stratosphere transport requires further studies.

[40] The simulations of the tropical lower stratosphere from NCAR WACCM3 and GFDL AMTRAC are compared with observations. The annual mean upward mass fluxes from both GCMs for the 40- to 30-hPa layer agree well with the observation, while the simulated mass fluxes for the 70- to 50-hPa layer are twice as larger. It is also found that the GCM simulated seasonal variation of the BDC agrees reasonably well with observations and reproduce the observed transition from an annual variation at 70–50 hPa to a semiannual variation at 40–30 hPa. However, neither GCM is capable of simulating the observed interannual variability of the BDC. Observations show that the interannual variability of the BDC is closely correlated with the QBO, which neither model represents. Comparisons of simulated temperatures, $H_2O$ and $O_3$ concentrations with those from observations suggest the intricate relation among these simulated quantities and the BDC and the accuracy of GCM radiation schemes in the lower stratosphere.

[41] Finally, despite the differences in the simulated ozone and water vapor, the AMTRAC and WACCM3 produce similar upward mass fluxes in the lower stratosphere, indicating the robustness of the conclusions drawn from the comparison between model and observational analyses. Further research is needed to understand why the models produce upward mass flux substantially larger than the observations in the lower level examined.

[42] **Acknowledgments.** We thank A.M. Thompson for useful discussions on the SHADOZ data. We thank Fumio Hasebe, Masato Shiotani, and Masatomo Fujiwara for their support of SOWER measurements. The ISCCP data are provided by the NASA Langley Research Center Atmospheric Sciences Data Center. Q.Y. thanks G. Anderson for the help on the MODTRAN4 software. This work is supported by the NASA grant NNX08AF66G.

## References

Alexander, M. J., and T. J. Dunkerton (1999), A spectral parameterization of mean flow forcing due to breaking gravity waves, *J. Atmos. Sci.*, *56*, 4167–4182, doi:10.1175/1520-0469(1999)056<4167:ASPOMF>2.0.CO;2.

Anderson, J. L., et al. (2004), The new GFDL global atmosphere and land model AM2/LM2: Evaluation with prescribed SST simulations, *J. Clim.*, *17*, 4641–4673.

Andrews, D. G., J. R. Holton, and C. B. Leovy (1987), *Middle Atmospheric Dynamics*, 498 pp., Academic, San Diego, Calif.

Austin, J., and N. Butchart (2003), Coupled chemistry-climate model simulations for the period 1980–2020: Ozone depletion and the start of ozone recovery, *Q. J. R. Meteorol. Soc.*, *129*, 3225–3249.

Austin, J., and J. Wilson (2006), Ensemble simulations of the decline and recovery of stratospheric ozone, *J. Geophys. Res.*, *111*, D16314, doi:10.1029/2005JD006907.

Boehm, M. T., and S. Lee (2003), The implications of tropical Rossby waves for tropical tropopause cirrus formation and for the equatorial upwelling of the Brewer-Dobson circulation, *J. Atmos. Sci.*, *60*, 247–261, doi:10.1175/1520-0469(2003)060<0247:TIOTRW>2.0.CO;2.

Brasseur, G. P., D. A. Hauglustaine, S. Walters, P. J. Rasch, J.-F. Müller, C. Granier, and X. X. Tie (1998), MOZART, a global chemical transport model for ozone and related chemical tracers: 1. Model description, *J. Geophys. Res.*, *103*, 28,265–28,290, doi:10.1029/98JD02397.

Brewer, A. W. (1949), Evidence for a world circulation provided by the measurements of helium and water vapor distribution in the stratosphere, *Q. J. R. Meteorol. Soc.*, *75*, 351–363, doi:10.1002/qj.49707532603.

Butchart, N., and A. A. Scaife (2001), Removal of chlorofluorocarbons by increased mass exchange between the stratosphere and troposphere in a changing climate, *Nature*, *410*, 799–802, doi:10.1038/35071047.

Butchart, N., et al. (2006), Simulations of anthropogenic change in the strength of the Brewer-Dobson circulation, *Clim. Dyn.*, *27*, 727–741, doi:10.1007/s00382-006-0162-4.

Chou, M., and M. Suarez (1999), A solar radiation parameterization for atmospheric studies, *NASA Tech. Rep., NASA/TM-1999–104606*, 40 pp.

Collins, W. D., et al. (2006), The formulation and atmospheric simulation of the Community Atmosphere Model: CAM3, *J. Clim.*, *19*, 2144–2161, doi:10.1175/JCLI3760.1.

Corti, T., B. P. Luo, T. Peter, H. Vomel, and Q. Fu (2005), Mean radiative energy balance and vertical mass fluxes in the equatorial upper troposphere and lower stratosphere, *Geophys. Res. Lett.*, *32*, L06802, doi:10.1029/2004GL021889.

Dobson, G. M. B. (1956), Origin and distribution of the polyatomic molecules in the atmosphere, *Proc. R. Soc., Ser. A*, *236*, 187–193, doi:10.1098/rspa.1956.0127.

Eichelberger, S. J., and D. L. Hartmann (2005), Changes in the strength of the Brewer-Dobson circulation in a simple AGCM, *Geophys. Res. Lett.*, *32*, L15807, doi:10.1029/2005GL022924.

Eluszkiewicz, J., et al. (1996), Residual circulation in the stratosphere and lower mesosphere as diagnosed from Microwave Limb Sounder data, *J. Atmos. Sci.*, *53*, 217–240, doi:10.1175/1520-0469(1996)053<0217:RCITSA>2.0.CO;2.

Eyring, V., et al. (2006), Assessment of temperature, trace species, and ozone in chemistry-climate model simulations of the recent past, *J. Geophys. Res.*, *111*, D22308, doi:10.1029/2006JD007327.

Folkins, I., P. Bernath, C. Boone, G. Lesins, N. Livesey, A. M. Thompson, K. Walker, and J. C. Witte (2006), Seasonal cycles of $O_3$, CO, and convective outflow at the tropical tropopause, *Geophys. Res. Lett.*, *33*, L16802, doi:10.1029/2006GL026602.

Fu, Q. (1996), An accurate parameterization of the solar radiative properties of cirrus clouds for climate models, *J. Clim.*, *9*, 2058–2082, doi:10.1175/1520-0442(1996)009<2058:AAPOTS>2.0.CO;2.

Fu, Q., and K. N. Liou (1992), On the correlated k-distribution method for radiative transfer in nonhomogeneous atmospheres, *J. Atmos. Sci.*, *49*, 2139–2156, doi:10.1175/1520-0469(1992)049<2139:OTCDMF>2.0.CO;2.

Fu, Q., and K. N. Liou (1993), Parameterization of the radiative properties of cirrus clouds, *J. Atmos. Sci.*, *50*, 2008–2025, doi:10.1175/1520-0469(1993)050<2008:POTRPO>2.0.CO;2.

Fu, Q., P. Yang, and W. B. Sun (1998), An accurate parameterization of the infrared radiative properties of cirrus clouds for climate models, *J. Clim.*, *11*, 2223–2237, doi:10.1175/1520-0442(1998)011<2223:AAPOTI>2.0.CO;2.

Fu, Q., Y. Hu, and Q. Yang (2007), Identifying the top of the tropical tropopause layer form vertical mass flux analysis and CALIPSO lidar cloud observations, *Geophys. Res. Lett.*, *34*, L14813, doi:10.1029/2007GL030099.

Fueglistaler, S., and Q. Fu (2006), Radiative heating rates in the tropical lower stratosphere over regions of persistent convection, *J. Geophys. Res.*, *111*, D23202, doi:10.1029/2006JD007273.

Garcia, R. R., D. R. Marsh, D. E. Kinnison, B. A. Boville, and F. Sassi (2007), Simulations of secular trends in the middle atmosphere, 1950–2003, *J. Geophys. Res.*, *112*, D09301, doi:10.1029/2006JD007485.

Gettelman, A., P. Forster, M. Fujiwara, Q. Fu, H. Vomel, L. Gohar, C. Johason, and M. Ammerman (2004), The radiation balance of the tropical tropopause layer, *J. Geophys. Res.*, *109*, D07103, doi:10.1029/2003JD004190.

Hartmann, D. L., L. A. Moy, and Q. Fu (2001), Tropical convection and the energy balance at the top of the atmosphere, *J. Clim.*, *14*, 4495–4511, doi:10.1175/1520-0442(2001)014<4495:TCATEB>2.0.CO;2.

Hasebe, F., H. Vömel, M. Shiotani, N. Nishi, S. Oltmans, T. Ogawa, and K. Gage (1999), First results from SOWER/Pacific, *SPARC Newsl.*, *12*, 22–23.

Haynes, P. H., M. E. McIntyre, T. G. Shepherd, C. J. Marks, and K. P. Shine (1991), On the "downward control" of extratropical diabatic circulations by eddy-induced mean zonal forces, *J. Atmos. Sci.*, *48*, 651–678, doi:10.1175/1520-0469(1991)048<0651:OTCOED>2.0.CO;2.

Hollars, S. C. (2004), Radiative regulations on cloud behaviors in the tropical western Pacific, M. S. thesis, Univ. of Wash., Seattle.

Holton, J. R., et al. (1995), Stratosphere-troposphere exchange, *Rev. Geophys.*, *33*, 403–439, doi:10.1029/95RG02097.

Horowitz, L. W., et al. (2003), A global simulation of tropospheric ozone and related tracers: Description and evaluation of MOZART, version 2, *J. Geophys. Res.*, *108*(D24), 4784, doi:10.1029/2002JD002853.

Kerr-Munslow, A. M., and W. A. Norton (2006), Tropical wave driving of the annual cycle in tropical tropopause temperatures. Part 1: ECMWF analyses, *J. Atmos. Sci.*, *63*, 1410–1419, doi:10.1175/JAS3697.1.

Kinnison, D. E., et al. (2007), Sensitivity of chemical tracers to meteorological parameters in the MOZART-3 chemical transport model, *J. Geophys. Res.*, *112*, D20302, doi:10.1029/2006JD007879.

Kley, D., J. M. Russell, and C. Philips (Eds.) (2000), Assessment of upper tropospheric and stratospheric water vapour, *WMO Tech. Doc. 1043*, 312 pp., World Meteorol. Org., Geneva.

Kratz, D., and F. Rose (1999), Accounting for molecular absorption within the spectral range of the CERES window channel, *J. Quant. Spectrosc. Radiat. Transfer*, *61*, 83–95, doi:10.1016/S0022-4073(97)00203-3.

Li, F., J. Austin, and J. Wilson (2008), The strength of the Brewer-Dobson circulation in a changing climate: Coupled chemistry-climate model simulations, *J. Clim.*, *21*, 40–57, doi:10.1175/2007JCLI1663.1.

Lin, S.-J. (2004), A "vertically Lagrangian" finite-volume dynamical core for global models, *Mon. Weather Rev.*, *132*, 2293–2307, doi:10.1175/1520-0493(2004)132<2293:AVLFDC>2.0.CO;2.

Liou, K. N. (1993), *Radiation and Cloud Processes in the Atmosphere*, 487 pp., Oxford Univ. Press, Oxford, U.K.

Liou, K., Q. Fu, and T. Ackerman (1988), A simple formulation of the delta-four-stream approximation for radiative transfer parameterizations, *J. Atmos. Sci.*, *45*, 1940–1947, doi:10.1175/15200469(1988)045<1940:ASFOTD>2.0.CO;2.

Mote, P. W., T. J. Dunkerton, M. E. McIntyre, E. A. Ray, P. H. Haynes, and J. M. Russell (1998), Vertical velocity, vertical diffusion, and dilution by midlatitude air in the tropical lower stratosphere, *J. Geophys. Res.*, *103*, 8651–8666, doi:10.1029/98JD00203.

Niwano, M., K. Yamazaki, and M. Shiotani (2003), Seasonal and QBO variations of the ascent rate in the tropical lower stratosphere as inferred from UARS HALOE trace gas data, *J. Geophys. Res.*, *108*(D24), 4794, doi:10.1029/2003JD003871.

Plumb, R. A. (1996), A "tropical pipe" model of stratospheric transport, *J. Geophys. Res.*, *101*, 3957–3972, doi:10.1029/95JD03002.

Plumb, R. A. (2002), Stratospheric transport, *J. Meteorol. Soc. Jpn.*, *80*, 793–809, doi:10.2151/jmsj.80.793.

Randel, W. J., F. Wu, R. Swinbank, J. Nash, and A. O'Neil (1999), Global QBO circulation derived from UKMO stratospheric analyses, *J. Atmos. Sci.*, *56*, 457–474, doi:10.1175/1520-0469(1999)056<0457:GQCDFU>2.0.CO;2.

Randel, W. J., R. R. Garcia, and F. Wu (2002), Time-dependent upwelling in the tropical lower stratosphere estimated from the zonal-mean momentum budget, *J. Atmos. Sci.*, *59*, 2141–2152, doi:10.1175/1520-0469(2002)059<2141:TDUITT>2.0.CO;2.

Randel, W. J., M. Park, F. Wu, and N. Livesey (2007), A large annual cycle in ozone above the tropical tropopause linked to the Brewer-Dobson circulation, *J. Atmos. Sci.*, *64*, 4479–4488, doi:10.1175/2007JAS2409.1.

Rind, D., D. Shindell, P. Lonergan, and N. K. Balachandran (1998), Climate change and the middle atmosphere. Part 3: The double $CO_2$ climate revisited, *J. Clim.*, *11*, 876–894, doi:10.1175/1520-0442(1998)011<0876:CCATMA>2.0.CO;2.

Rose, F., and T. P. Charlock (2002), New Fu-Liou code tested with ARM Ramen lidar and CERES in pre-CALIPSO exercise, paper presented at 11th Conference on Atmospheric Radiation, Am. Meteorol. Soc., Ogden, Utah.

Rosenlof, K. H. (1995), Seasonal cycle of the residual mean meridional circulation in the stratosphere, *J. Geophys. Res.*, *100*, 5173–5191, doi:10.1029/94JD03122.

Rosenlof, K. H., and J. R. Holton (1993), Estimate of the stratospheric residual circulation using the downward control principle, *J. Geophys. Res.*, *98*, 10,465–10,479, doi:10.1029/93JD00392.

Rossow, W. B., and R. A. Schiffer (1999), Advances in understanding clouds from ISCCP, *Bull. Am. Meteorol. Soc.*, *80*, 2261–2287, doi:10.1175/1520-0477(1999)080<2261:AIUCFI>2.0.CO;2.

Russell, J. M., et al. (1993), The halogen occultation experiment, *J. Geophys. Res.*, *98*, 10,777–10,797, doi:10.1029/93JD00799.

Slingo, A. (1989), A GCM parameterization for the shortwave radiative properties of water clouds, *J. Atmos. Sci.*, *46*, 1419–1427, doi:10.1175/1520-0469(1989)046<1419:AGPFTS>2.0.CO;2.

Smit, H. G. J., et al. (2007), Assessment of the performance of ECC-ozonesondes under quasi-flight conditions in the environment chamber: Insights from the Juelich Ozone Sonde Intercomparison Experiment (JOSIE), *J. Geophys. Res.*, *112*, D19306, doi:10.1029/2006JD007308.

Solomon, S., J. T. Kiehl, P. R. Garcia, and W. Grose (1986), Tracer transport by the diabatic circulation deduced from satellite observations, *J. Atmos. Sci.*, *43*, 1603–1617, doi:10.1175/1520-0469(1986)043<1603:TTBTDC>2.0.CO;2.

Swinbank, R., and A. O'Neill (1994), A stratosphere-troposphere data assimilation system, *Mon. Weather Rev.*, *122*, 686–702, doi:10.1175/1520-0493(1994)122<0686:ASTDAS>2.0.CO;2.

Thompson, A. M., et al. (2003), Southern Hemisphere Additional Ozonesondes (SHADOZ) 1998–2000 tropical ozone climatology: 1. Comparison with Total Ozone Mapping Spectrometer (TOMS) and ground-based measurements, *J. Geophys. Res.*, *108*(D2), 8238, doi:10.1029/2001JD000967.

Thompson, A. M., J. C. Witte, H. G. J. Smit, S. J. Oltmans, B. J. Johnson, V. W. J. H. Kirchhoff, and F. J. Schmidlin (2007), Southern Hemisphere Additional Ozonesondes (SHADOZ) 1998–2004 tropical ozone climatology: 3. Instrumentation, station-to-station variability, and evaluation with simulated flight profiles, *J. Geophys. Res.*, *112*, D03304, doi:10.1029/2005JD007042.

Tobin, D., et al. (1999), Downwelling spectral radiance observations at the Sheba ice station: Water vapor continuum measurements from 17 to 26 $\mu$m, *J. Geophys. Res.*, *104*, 2081–2092, doi:10.1029/1998JD200057.

Vömel, H., et al. (2002), Balloon-borne observations of water vapor and ozone in the tropical upper troposphere and lower stratosphere, *J. Geophys. Res.*, *107*(D14), 4210, doi:10.1029/2001JD000707.

J. Austin, Geophysical Fluid Dynamics Laboratory, Princeton, NJ 08542, USA.

Q. Fu and Q. Yang, Department of Atmospheric Sciences, University of Washington, Seattle, WA 98195, USA. (qyang@atmos.washington.edu)

A. Gettelman, National Center for Atmospheric Research, Boulder, CO 80305, USA.

F. Li, Goddard Earth Sciences and Technology Center, University of Maryland, Baltimore County, Baltimore, MD 21250, USA.

H. Vömel, Cooperative Institute for Research in Environmental Sciences, University of Colorado, Boulder, CO 80309, USA.